PROCEEDINGS, 49th Workshop on Geothermal Reservoir Engineering
Stanford University, Stanford, California, February 12-14, 2024
SGP-TR-227

WHOLESCALE modeling of thermo-hydro-mechanical processes at San Emidio, Nevada, U.S. on time scales of years

Kurt L. Feigl (1), Xi Luo (1), Chris Sherman (2), Corné Kreemer (3), Sam A. Batzli (1), Michael A. Cardiff (1), and Herbert F. Wang (1)

(1) University of Wisconsin-Madison, Madison, WI, United States;
(2) Lawrence Livermore National Laboratory, Livermore, CA, United States;
(3) University of Nevada Reno, NV, United States;

feigl@wisc.edu

ABSTRACT

The WHOLESCALE acronym stands for Water & Hole Observations Leverage Effective Stress Calculations and Lessen Expenses. The goal of the WHOLESCALE project is to simulate the spatial distribution and temporal evolution of stress in the geothermal system at San Emidio in Nevada, United States. To reach this goal, the WHOLESCALE team is developing a fully coupled, thermo-hydro-mechanical ("T-H-M") numerical model to describe geodetic observations during the shutdowns using the open-source GEOS code developed at Lawrence Livermore National Laboratory (Settgast et al., 2018). In refining the models, we consider two different time scales. In this paper, we focus on long time scales of the order of years. In a companion paper (Luo et al., 2024), we consider short time scales on the order of minutes to days.

To calibrate the model, we consider two types of geodetic data: GPS (Global Positioning System) and InSAR (Interferometric Synthetic Aperture Radar). The GPS data set consists of daily time series of displacement in three dimensions. These have been estimated from data collected from two continuously operating stations, SEMS and SEMN, installed on monuments attached to idle wellheads within the geothermal field at San Emidio as well as from a third GPS station, named GARL, located outside the geothermal area in the mountain range to the northeast of the power plant.

The shape of the modeled displacement field agrees approximately with that observed by InSAR near the producing wells at the center of the geothermal field. The modeled rate of vertical displacement, however, agrees with that estimated from GPS and InSAR data only to within a factor of four.

Keywords: WHOLESCALE, San Emidio, EGS, GPS, INSAR, FEM

INTRODUCTION

The San Emidio geothermal area is located ~100 km north of Reno, Nevada in the northwestern Basin and Range province, as described previously (Matlick, 1995; Rhodes et al., 2010; Warren, 2010; Eneva et al., 2011; Moeck, 2011; Rhodes, 2011; Rhodes et al., 2011; Faulds, 2014; UNR, 2014; Teplow and Warren, 2015; Pulliam et al., 2019; Reinisch et al., 2019; Warren et al., 2019; Feigl et al., 2020; Folsom et al., 2020; Folsom et al., 2021; Feigl et al., 2022; Guo et al., 2022; Jahnke, 2022; Jahnke et al., 2022; Akerley et al., 2023; Jahnke et al., 2023; Sone et al., 2023).

The San Emidio geothermal system occupies a right step in a North-striking, West-dipping, normal fault zone. Minor dilation and high fault density within the right step likely produce the permeability necessary for deep fluid circulation (e.g., Eneva et al., 2011). Power was first produced in 1987 with a 3.6-MW binary plant, and average production increased to 9 MW (net) following commissioning of a new power plant in 2012. Production has ranged from less than 190 L/s to more than 280 L/s at temperatures of 140–148°C. Drilling, geological, geophysical, and geochemical data sets collected since the 1970s help constrain controls on the geothermal resource and the structural setting. The data sets include historic drilling records, magnetotelluric resistivity, seismic reflection imaging, passive seismic emission tomography (PSET), microseismicity analysis, and gravimetric surveys. Figure 1 shows a conceptual model in vertical cross section.

Our WHOLESCALE team includes researchers at two universities and two national laboratories working in a public-private partnership with Ormat Technologies Inc. The goal of the WHOLESCALE project is to simulate the spatial distribution and temporal evolution of stress in a geothermal system. To reach this goal, the WHOLESCALE team is developing a methodology to incorporate and interpret data into a multi-physics model that couples thermal, hydrological, and mechanical (T-H-M) processes over spatial scales ranging from ~100 m to ~5 km and temporal scales ranging from ~1 days to ~10 years.

Accordingly, the WHOLESCALE team is analyzing multiple types of observational data at San Emidio, measuring material properties of San Emidio rock samples in our laboratory and performing simulations with a multiphysics T-H-M modeling code named GEOS that has been developed at Lawrence Livermore National Laboratory. In this paper, we focus on simulating deformation of the land surface over time scales spanning years. The goal is to simulate the deformation field measured by the Global Positioning System (GPS) and Interferometric Synthetic Aperture Radar (InSAR).

DATA

Geodesy

Geodesy measures deformation of the ground surface. Two continuously operating GPS stations, SEMS and SEMN, have been installed on monuments attached to idle wellheads within the geothermal field at San Emidio. GPS station SEMS was installed on the head of idle Well 17-21 at the southern edge of the geothermal field in January 2021 and then removed in April 2022. GPS station SEMN was installed on the head of idle Well 65C-16 near the power plant locate at center of the geothermal field in January 2021. A third GPS station, named GARL, is located outside the geothermal area in the mountain range to the northeast of the power plant to provide a stable reference point. We analyze the GPS data to calculate daily measurements of (relative) position coordinates in three dimensions that can be modeled as time series of displacement (Blewitt et al., 2018; Kreemer et al., 2020).

Interferometric Synthetic Aperture Radar (InSAR) data also measures ground deformation. The data set includes InSAR data collected by several satellite missions. The ERS-1/2 missions operated by the European Space Agency acquired image data covering San Emidio over two distinct time intervals 1992 to 2001 and 2003 to 2010, respectively (Eneva et al., 2011). These authors found relative rates of line-of-sight (LOS) displacement of the order of 5 mm/year at locations near the power plant at San Emidio. Assuming that the motion is purely vertically downward (subsidence) and dividing by the cosine of the incidence angle (~23°), we infer that the rate of vertical displacement is approximately 5.4 mm/year with respect to a location outside the geothermal field. By modeling the same two data sets, Reinisch et al. (2019) conclude that the rate of deformation was constant between 1992 and 2010.

A second InSAR data set consists of radar images acquired monthly beginning in 2019 by the TerraSAR-X (Pitz and Miller, 2010)and TanDEM-X (Krieger et al., 2007)satellite missions operated by the German Space Agency (DLR). To analyze these data, we have developed a high-throughput workflow using HT-Condor (Reinisch, 2018b; Reinisch, 2018a)to apply the GMT-SAR processingsoftware (Sandwell et al., 2011; Sandwell et al., 2016).

We are also analyzing InSAR data from the SENTINEL-1 satellite mission (Salvi et al., 2012)operated by the European Space Agency (ESA). These data sets cover the site from late 2014 through the present. For the data acquired by the SENTINEL missions, we use the geocoded interferograms (standard InSAR displacement – GUNW – products) calculated by the Advanced Rapid Imaging and Analysis (ARIA) project (Bekaert et al., 2019).

To analyze the interferometric pairs as time series of displacement, we use the Miami INsar Time-series software in PYthon (MintPy) workflow (Yunjun et al., 2019). Figure 2, Figure 3, and Figure 4 show maps of the vertical displacement estimated from InSAR for three data sets acquired by the Sentinel-1 mission at different dates between 2016 and 2023. Each of the three data sets shows relative subsidence (blue colors) faster than 3 mm/year in absolute value in three areas:

Area A: Near the center of the geothermal field near GPS station SEMN (mapped as a yellow square), the deformation field shows a 3-km-by-2-km lobe of subsidence with a maximum rate of downward vertical displacement of ~5 mm/year in absolute value.

Area B: In the northwest corner of the map, deformation field shows a circular area approximately 1 km in radius where the maximum rate of downward vertical displacement is ~10 mm/year in absolute value. This feature is located within a kilometer of a circular "pivot sprinkler" irrigation system. We interpret the deformation as subsidence resulting from pumping groundwater from a shallow aquifer. Area B is not covered by the GEOS modeling.

Area C: Over the dry lake bed ("playa") to the west of GPS station SEMN, we see a lobe of subsidence centered at (X,Y) = (7, 16) [km]. Here, the displacement rate is significantly different from zero with 99% confidence only in Figure 2 and Figure 3.

Before attemptingto simulate these observations quantitatively, we consider four possible interpretations.

In the first interpretation, the subsiding "bowls" observed near the irrigation system (Area A) and geothermal wells (Area B) are related to pumping fluids into or out of the wells. To explain the observed subsidence in Area B over an area roughly ~2 km in diameter, however, would require a "sink" that shrinks in volume at a depth of the order of a kilometer. Whether the volumetric contraction is due to the hydro-mechanical (H-M) processes or thermo-mechanical (T-M) processes is a question that we begin to address using numerical modeling below.

In the second interpretation, the signatures observed in the InSAR data could be related to changes in soil moisture (e.g., Zan et al., 2015; Ansari et al., 2017; Zheng et al., 2022). This effect could be pronounced on the dry lake bed (Area B) to the west of the geothermal field, where rainfall is rare. Considering a time series of Sentinel-1 data acquired near Bristol Dry Lake in the Barstow-Bristol Trough region of California, Zheng et al. (2022) write that "the bias time series of a pixel on the edge of the Bristol dry lake show clear correlation with precipitation and 'may' indicate the InSAR phase response to the drying process of soil after precipitation" (Zheng et al., 2022; emphasis theirs). Changes in soil moisture could affect the InSAR results near the agricultural fields around the circular irrigation system, as also noted around irrigated agricultural fields in the Imperial Valley of California (Gabriel et al., 1989).

In the third interpretation, the signatures observed in the InSAR results could be artefacts related to the time series analysis. In some cases, applying spatial averaging (so-called "multi-looking") to Synthetic Aperture Radar (SAR) images may cause a systematic bias in deformation modeling (e.g., Xu and Sandwell, 2020; Zheng et al., 2022).

In the fourth interpretation, the signatures observed in the InSAR data could be related to atmospheric effects. Heterogeneities in the atmosphere perturb the radar signals as they propagate along the "line of sight" between the sensor aboard the spacecraft in orbit to the

ground and back again. As sketched by Massonnet and Feigl (1998) in their Figure 7, this effect produces a larger delay for a pixel located at a low elevation than for a pixel located at a high elevation. This effect has several nicknames, including "inverted barometer", "tropo-topo", and "height-correlation". To mitigate the effect of such atmospheric perturbations, we consider several different approaches. The first approach neglects atmospheric effects. In the second approach, we assume a horizontally stratified atmosphere, such that the delay is proportional to the difference in topographic elevation between two pixels in distinct locations. The algorithm (Berrada Baby et al., 1988) is implemented in MintPy with the "height_correlation" key word. The third approach uses weather data assimilated into meteorologic models from the European Centre for Medium-Range Weather Forecasts (ECWMF) to simulate the atmospheric delay. To trace rays through the atmospheric models, we use the Python based Atmospheric Phase Screen — PyAPS (Jolivet et al., 2015).

Which interpretation is correct? To address this question, we compare the InSAR results with time series of vector displacement at GPS stations. To minimize the effects of different reference frames, we consider differential displacement of GPS stations SEMN with respect to SEMS. To calculate the vertical component of displacement field from the InSAR results, we assume that the displacement is purely vertical. In other words, we divide the line-of-sight (LOS) displacements (and their rates) by the cosine of the incidence angle.

Figure 5 shows the time series of relative vertical displacement estimated from InSAR data for a pixel located near GPS station SEMN with respect to a pixel located near GPS station SEMS for InSAR data acquired in Sentinel-1 Tracks 64 and 42, respectively.

The time series of vertical component of displacement estimated from GPS data at station SEMN with respect to SEMS is also shown (identically) in each of these two panels. For the GPS data, we perform a weighted least-squares fit to estimate the rate of vertical displacement. For the InSAR data, we estimate the rate of vertical displacement using an unweighted least-squares fit as well as showing the average velocity estimated using MintPy. In each case, the quoted uncertainty in rate represents a formal estimate of one standard deviation scaled by the square root of the (weighted) mean squared error (WMSE). For Track 42, the rate of relative vertical displacement estimated from the InSAR data by MintPy is -7.5 ± 0.2 mm/year (downward). This estimate differs by less than 1 mm/year from the rate of -7.6 ± 0.4 mm/year estimated from the GPS data by a least-squares fit. For Track 144, the rate of relative vertical displacement estimated from the InSAR data by MintPy is -3.5 ± 0.1 mm/year (downward). This rate differs significantly from the rate estimated from the GPS data.

The quoted standard errors are formal. The procedure used to estimate the rate of vertical displacement from the GPS data does not account for temporal correlations between successive days of GPS measurements. Similarly, the procedure used to estimate the rate of vertical displacement from the InSAR data does not account for the correlation between two interferometric pairs that share a common acquisition date. These effects tend to increase the uncertainty of the estimated rates (e.g., Agram and Simons, 2015; Reinisch et al., 2016). The displacement rate of SEMN with respect to SEMS is –7.0 ± 2.3 mm/year estimated from the GPS data using the MIDAS robust trend estimator (Blewitt et al., 2016). Consequently, we consider that a more realistic estimate of the standard error of the vertical displacement rate is at least 2 mm/year.

We consider the InSAR results from Sentinel-1 Track 42 (Figure 2) to be the most reliable data set for interpretation because the rates of vertical displacement estimated from GPS agree more closely with the InSAR rates for Track 42 than for Track 64.

Which approach to mitigating atmospheric effects is most reliable? To address this question, we again compare the rates estimated from InSAR data to those estimated from GPS data. Figure 6 shows the comparison for each of the three approaches. The results using the height-correlation approach (-7.2 ± 0.2 mm/year, upper panel) insignificantly different from those estimated without accounting for atmospheric effects (-7.5 ± 0.2 mm/year, middle panel). The latter estimate differs by less than 0.1 mm/year from the rate of -7.6 ± 0.4 mm/year estimated from the GPS data by a least-squares fit. In contrast, however, using the PyAPS approach with meteorological data yields an estimated rate of 0.0 ± 0.1 mm/year (lower panel). Consequently, we consider only the displacement rate estimated without accounting for atmospheric effects in the subsequent interpretation.

T-H-M modeling

We are developing a fully coupled, thermo-hydro-mechanical ("T-H-M") numerical model using the open-source GEOS code developed at Lawrence Livermore National Laboratory (e.g., Liu et al., 2018; Settgast et al., 2018). To constrain the modeling effort, the WHOLESCALE team is analyzing multiple types of observational data at San Emidio. Our long-term T-H-M modeling uses the same set of finite elements in the tessellated mesh of tetrahedral elements as described by Luo et al. (2024, this meeting). For the mechanical and hydrologic aspects of the model, we use the same material properties, initial conditions, and boundary conditions as assumed for the short-term H-M model (Luo et al., 2024). The modeled viscosity of water is assumed to be constant, i.e. it does not vary with temperature. For the thermal aspects of the modeling, the material properties are listed in Table 1 and the boundary conditions are listed in Table 2. The initial conditions are set to the "natural state" temperatures before production began shown as red contours in Figure 1 (Folsom et al., 2022). The modeling results in terms of vertical displacement rate are shown in map view (Figure 7) and time series (Figure 8).

DISCUSSION

Following the presentation of the geodetic measurements of deformation as observed by InSAR and GPS and the modeling results from GEOS, we compare the latter to the former.

In Area C, on the playa to the west of the production wells, the modeled deformation field (Figure 7) differs markedly from the deformation field observed by InSAR (Figure 3). The observed deformation field shows a velocity gradient greater than 1 mm/year per kilometer where the modeled displacement field is essentially uniformly less than 2 mm/year.

In Area A, near the production wells, the shape of the modeled subsidence "bowl" (Figure 7) roughly mimics that observed by InSAR in Sentinel-1 Track 42 (Figure 3). The modeled rate of vertical displacement, however, is significantly higher than the observed rate. To quantify this difference, we consider the (relative) vertical displacement of a point located in the center of the geothermal field (near GPS station SEMN) with respect to a point located at the southern edge of the geothermal field (near GPS station SEMS). This rate is –28.2 ± 0.1 mm/year in the model (Figure 8). The InSAR estimate is –7.5 ± 0.2 mm/year, as estimated from InSAR data acquired between 2016-01-07 and 2022-06-04 in Sentinel-1 Track 42 without accounting for atmospheric effects (yellow circles in upper panel of Figure 6). The InSAR estimate agrees well with the value of –7.6 ± 0.4 mm/year estimated from the GPS data between January 2021 and April 2022 by a least-squares fit (red points with error bars Figure 6). A realistic estimate of the uncertainty on both geodetic rates is more likely to be of the order of 2 mm/year.

CONCLUSIONS

The shape of the modeled displacement field agrees approximately with that observed by InSAR near the producing wells at the center of the geothermal field. The modeled rate of vertical displacement, however, agrees with that estimated from GPS and InSAR data only to within a factor of four. Further tuning of the model parameters, especially spatial permeability, will be required to match the geodetic observations.

ACKNOWLEDGMENTS

The WHOLESCALE team thanks the following individuals at Ormat: Curtis Peach, Cliff Reed, Joe Pavone, Manolo Di Donato, Leeta Miller, Alan Pinuelas-Molina, David Schwab, Lupé Gonsalez Ortiz, Gabrielle Ramirez, Courtney Brailo, John Murphy, and Robin Zuza. We also acknowledge the data shared by Ormat Technologies, Inc.

Some of the figures in this paper were generated using Leapfrog Geothermal Software Leapfrog (Bentley Systems, Incorporated).

Passive seismic data collections were completed at San Emidio in late 2016 by Microseismic Inc. as part of DOE project number DE-EE0007698 as described at https://gdr.openei.org/submissions/1386

The work presented herein has been funded in part by the Office of Energy Efficiency and Renewable Energy (EERE), U.S. Department of Energy, under Award Numbers DE-EE0007698 and DE-EE0009032. Parts of this work were performed under the auspices of the U.S. Department of Energy by Lawrence Livermore National Laboratory under Contract DE-AC52-07NA27344.

REFERENCES

Agram, P. S., and M. Simons (2015), A noise model for InSAR time-series, Journal of Geophysical Research: Solid Earth, 2014JB011271. http://dx.doi.org/10.1002/2014JB011271

Akerley, J., I. Warren, E. Gasperikova, and S. Pullammanappallil (2023), A Novel Approach to Map Permeability Using Passive Seismic Emission Tomography, United States. https://www.osti.gov/biblio/1986084

Ansari, H., F. D. Zan, and R. Bamler (2017), Sequential Estimator: Toward Efficient InSAR Time Series Analysis, IEEE Transactions on Geoscience and Remote Sensing, 55, 5637-5652.

Bekaert, D. P., M. Karim, J. P. Linick, H. Hua, S. Sangha, M. Lucas, N. Malarout, P. S. Agram, L. Pan, and S. E. Owen (2019), Development of open-access Standardized InSAR Displacement Products by the Advanced Rapid Imaging and Analysis (ARIA) Project for Natural Hazards, paper presented at AGU Fall Meeting Abstracts.

Berrada Baby, H., P. Golé, and J. Lavergnat (1988), A model for the tropospheric excess path length of radio waves from surface meteorological measurements, Radio Science, 23, 1023-1038. https://doi.org/10.1029/RS023i006p01023

Blewitt, G., C. Kreemer, W. C. Hammond, and J. Gazeaux (2016), MIDAS robust trend estimator for accurate GPS station velocities without step detection, Journal of Geophysical Research: Solid Earth, 121, 2054-2068. https://doi.org/10.1002/2015JB012552

Blewitt, G., W. C. Hammond, and C. Kreemer (2018), Harnessing the GPS Data Explosion for Interdisciplinary Science, Eos, 99. https://doi.org/10.1029/2018EO104623

Eneva, M., G. Falorni, W. Teplow, J. Morgan, G. Rhodes, and D. Adams (2011), Surface Deformation at the San Emidio Geothermal Field, Nevada, from Satellite Radar Interferometry, GRC Transactions, 35.

Faulds, J. E. (2014), 3D Model of the San Emidio Geothermal Area [data set], Geothermal Data Repository. https://gdr.openei.org/submissions/365.

Feigl, K. L., E. C. Reinisch, S. A. Batzli, H. Sone, M. A. Cardiff, J. C. Hampton, N. E. Lord, C. H. Thurber, H. F. Wang, and C. Sherman (2020), Spatio–Temporal Analysis of Deformation at San Emidio Geothermal Field, Nevada, USA between 1992 and 2010, paper presented at Proceedings 45th Workshop on Geothermal Reservoir Engineering Stanford University, Stanford, California, February 10-12, 2020. https://pangea.stanford.edu/ERE/db/GeoConf/papers/SGW/2020/Feigl.pdf

Feigl, K. L., S. Tung, H. Guo, E. Cunningham, J. Hampton, S. J. Kleich, B. Jahnke, B. Heath, C. Roland, M. Folsom, J. Akerley, M. Cusini, C. Sherman, I. Warren, C. Kreemer, H. Sone, M. A. Cardiff, N. E. Lord, C. H. Thurber, and H. F. Wang (2022), Overview and Preliminary Results from the WHOLESCALE project at San Emidio, Nevada, U.S., paper presented at 47th Workshop on Geothermal Reservoir Engineering, Stanford, California. https://pangea.stanford.edu/ERE/pdf/IGAstandard/SGW/2022/Feigl.pdf

Folsom, M., R. Libbey, D. Feucht, W. I., and S. Garanzini (2020), Geophysical Observations and Integrated Conceptual Models of the San Emidio Geothermal Field, Nevada., paper presented at Workshop on Geothermal Reservoir Engineering, Stanford, California, USA. https://pangea.stanford.edu/ERE/db/GeoConf/papers/SGW/2020/Folsom.pdf

Folsom, M., R. Libbey, D. Feucht, I. Warren, and S. Garanzini (2021), Geophysical observations and integrated conceptual models of the San Emidio Geothermal Field, Nevada, paper presented at Nevada Petroleum & Geothermal Society, February 4th, 2021.

Gabriel, A. K., R. M. Goldstein, and H. A. Zebker (1989), Mapping small elevation changes over large areas: differential radar interferometry, J. Geophys. Res., 94, 9183-9191.

Guo, H., C. H. Thurber, B. A. Heath, M. Cardiff, N. Lord, I. Warren, and K. L. Feigl (2022 of Conference), Seismic analysis of reservoir conditions for inducing seismicity at the San Emidio geothermal field, Nevada, U.S.A., abstract presented at Annual Meeting Seismological Society of America, Bellevue, WA, USA, 19-23 April 2022.

Jahnke, B. (2022), Geomechanical Analysis of the Geothermal Reservoir at San Emidio, Nevada and Fracture Toughness Anisotropy of EGS Collab Testbed Rocks, M.S. thesis thesis, University of Wisconsin-Madison (H. Sone, advisor).

Jahnke, B., H. Guo, B. Heath, E. Cunningham, C. Sherman, H. Sone, I. Warren, C. Kreemer, C. H. Thurber, K. F. Feigl, and WHOLESCALE_Team (2022), Spatial-Temporal Stress Heterogeneity in the Geothermal Reservoir at San Emidio, Nevada, U.S., paper presented at 45th Workshop on Geothermal Reservoir Engineering, February 7-9, 2022, Stanford University, Stanford, California,. https://pangea.stanford.edu/ERE/pdf/IGAstandard/SGW/2022/Jahnke.pdf

Jahnke, B., H. Sone, H. Guo, C. Sherman, I. Warren, C. Kreemer, C. H. Thurber, and K. L. Feigl (2023), Geomechanical analysis of the geothermal reservoir at San Emidio, Nevada, Geothermics, 110, 102683. https://doi.org/10.1016/j.geothermics.2023.102683

Jolivet, R., M. Simons, P. S. Agram, Z. Duputel, and Z. K. Shen (2015), Aseismic slip and seismogenic coupling along the central San Andreas Fault, Geophysical Research Letters, 42, 297-306. http://dx.doi.org/10.1002/2014GL062222

Kreemer, C., G. Blewitt, and P. Davis (2020), Geodetic evidence for a buoyant mantle plume beneath the Eifel volcanic area, NW Europe, Geophysical Journal International, 222., 1316-1332. https://doi.org/10.1093/gji/ggaa227

Krieger, G., A. Moreira, H. Fiedler, I. Hajnsek, M. Werner, M. Younis, and M. Zink (2007), TanDEM-X: A Satellite Formation for High-Resolution SAR Interferometry, IEEE Trans. Geoscience Remote Sensing, 45, 3317-3341. http://dx.doi.org/10.1109/tgrs.2007.900693

Liu, F., P. Fu, R. J. Mellors, M. A. Plummer, S. T. Ali, E. C. Reinisch, Q. Liu, and K. L. Feigl (2018), Inferring Geothermal Reservoir Processes at the Raft River Geothermal Field, Idaho, USA, Through Modeling InSAR-Measured Surface Deformation, Journal of Geophysical Research: Solid Earth, 123, 3645-3666. http://dx.doi.org/10.1029/2017JB015223

Luo, X., C. Sherman, K. L. Feigl, H. Sone, M. A. Cardiff, J. Hampton, H. Guo, N. E. Lord, P. E. Sobol, C. H. Thurber, and H. F. Wang (2024), WHOLESCALE Modeling of Hydro-Mechanical Processes at San Emidio, Nevada, U.S. on Time Scales of Days, 48th Workshop on Geothermal Reservoir Engineering, Stanford, California February 6-8, 2024.

Massonnet, D., and K. L. Feigl (1998), Radar interferometry and its application to changes in the Earth's surface, Reviews of Geophysics, 36, 441-500. https://doi.org/10.1029/97RG03139

Matlick, J. S. (1995), San Emidio Geothermal System, Empire, Nevada: GRC Field Trip ~ October 1995, Mesquite Group, Inc., Fullerton, California. https://data.nbmg.unr.edu/public/Geothermal/Grey Literature/Matlick_SanEmidioGeoSystem_1995.pdf

Moeck, I. (2011), Stress Inversion and 2D fault stress modeling San Emidio: Project Report to PI Teplow, 19 page pp.

Pitz, W., and D. Miller (2010), The TerraSAR-X Satellite, Geoscience and Remote Sensing, IEEE Transactions on, 48, 615-622. http://dx.doi.org/10.1109/TGRS.2009.2037432

Pulliam, R. J., F. Sepulveda, J. S. Thangraj, D. Quiros, J. Queen, M. Queen, and J. Iovenitti (2019), Development of a Novel, Near Real Time Approach To Geothermal Seismic Exploration And Monitoring Via Ambient Seismic Noise Interferometry, Medium: ED pp, Baylor Univ., Waco, TX (United States). https://www.osti.gov/servlets/purl/1648329

Reinisch, E. C., M. Cardiff, and K. L. Feigl (2016), Graph theory for analyzing pair-wise data: application to geophysical model parameters estimated from interferometric synthetic aperture radar data at Okmok volcano, Alaska, Journal of Geodesy, 1-16. http://dx.doi.org/10.1007/s00190-016-0934-5

Reinisch, E. C. (2018a), UW Madison HTCondor InSAR Workflow (Source Code). https://github.com/ecreinisch/bin_htcondor.git

Reinisch, E. C. (2018b), UW Madison HTCondor InSAR Workflow (User Manual). https://uwmadison.app.box.com/v/HTCondorInSARWorkflowManual

Reinisch, E. C., M. Cardiff, J. Akerley, I. Warren, and K. L. Feigl (2019), Spatio–Temporal Analysis of Deformation at San Emidio Geothermal Field, Nevada, USA Between 1992 and 2010, Remote Sensing, 11, 1935. http://dx.doi.org/10.3390/rs11161935

Rhodes, G. T., J. E. Faulds, and W. Teplow (2010), Structural Controls of the San Emidio Desert Geothermal Field, Northwestern Nevada, paper presented at Geothermal Resource Council Transactions.

Rhodes, G. T. (2011), Structural controls of the San Emidio Geothermal System, M.S. thesis, vi, 73 leaves pp, University of Nevada Reno advisor).

Rhodes, G. T., J. E. Faulds, and A. R. Ramelli (2011), Preliminary Geologic Map of the Northern Lake Range, San Emidio Geothermal Area, Washoe County, Nevada, Nevada Bureau of Mines and Geology. http://data.nbmg.unr.edu/public/freedownloads/of/of2011-11.zip

Salvi, S., S. Stramondo, G. J. Funning, A. Ferretti, F. Sarti, and A. Mouratidis (2012), The Sentinel-1 mission for the improvement of the scientific understanding and the operational monitoring of the seismic cycle, Remote Sensing of Environment, 120, 164-174. http://dx.doi.org/10.1016/j.rse.2011.09.029

Sandwell, D., R. Mellors, X. Tong, M. Wei, and P. Wessel (2011), Open radar interferometry software for mapping surface deformation, Eos, Transactions American Geophysical Union, 92, 234-234. http://topex.ucsd.edu/gmtsar

Sandwell, D., R. Mellors, X. Tong, X. Xu, M. Wei, and P. Wessel (2016), GMTSAR: An InSAR Processing System Based on Generic MappingTools., UC San Diego: Scripps Institution of Oceanography. http://topex.ucsd.edu/gmtsar/tar/GMTSAR_2ND_TEX.pdf

Settgast, R. R., J. A. White, B. C. Corbett, A. Vargas, C. Sherman, P. Fu, and C. Annavarapu (2018), GEOSX Simulation Framework: General multi-physics simulation framework targeting exascale computing platforms, Medium: X; OS: Any pp., Lawrence Livermore National Lab. (LLNL), Livermore, CA (United States). https://www.osti.gov/biblio/1422506

Sone, H., Z. Jin, O. Mudatsir, I. Warren, M. Folsom, and K. L. Feigl (2023), WHOLESCALE - Characterization of Conductive Fractured Zones Based on Borehole Data at San Emidio Geothermal Field, Nevada, paper presented at Stanford Geothermal Workshop. https://pangea.stanford.edu/ERE/db/GeoConf/papers/SGW/2023/Sone.pdf

Teplow, W. J., and I. Warren (2015), Finding Large Aperture Fractures in Geothermal Resource Areas Using a Three-Component Long-Offset Surface Seismic Survey, PSInSAR and Kinematic Structural Analysis, Medium: ED; Size: 52 p. pp, US Geothermal, Inc., Boise, ID (United States). https://doi.org/10.2172/1213113

UNR (2014), Slip and Dilation Tendency Analysis of the San Emidio Geothermal Area [data set]. https://gdr.openei.org/submissions/371

Warren, I. (2010), Three-Component Long Offset Surface Seismic Survey Data Used to Find Large Aperture Fractures in Geothermal Resources - San Emidio Geothermal Resource Area, U.S. Geothermal Inc. https://doi.org/10.15121/1422726

Warren, I., E. Gasperikova, and S. Pullammanappallil (2019), Final Phase 1 Report DE-EE0007698: A Novel Approach to Map Permeability Using Passive Seismic Emission Tomography. https://subterraseis.com/wp-content/uploads/2019/10/Doc1.pdf

Xu, X., and D. T. Sandwell (2020), Toward Absolute Phase Change Recovery With InSAR: Correcting for Earth Tides and Phase Unwrapping Ambiguities, IEEE Transactions on Geoscience and Remote Sensing, 58, 726-733. https://ieeexplore.ieee.org/document/8850313/

Yunjun, Z., H. Fattahi, and F. Amelung (2019), Small baseline InSAR time series analysis: Unwrapping error correction and noise reduction, Computers & Geosciences, 133.

Zan, F. D., M. Zonno, and P. López-Dekker (2015), Phase Inconsistencies and Multiple Scattering in SAR Interferometry, IEEE Transactions on Geoscience and Remote Sensing, 53, 6608-6616.

Zheng, Y., H. Fattahi, P. Agram, M. Simons, and P. Rosen (2022), On Closure Phase and Systematic Bias in Multilooked SAR Interferometry, IEEE Transactions on Geoscience and Remote Sensing, 60, 1-11.

Table 1. Material properties for each set of elements.

# name	fieldName	component	scale	unit
initialTemperature	temperature	NA	0	K
thermal_expansion_QTA	rock_thermalExpansionCoefficient	NA	1.50E-05	1/K
thermal_expansion_QAS	rock_thermalExpansionCoefficient	NA	1.50E-05	1/K
thermal_expansion_TPTS	rock_thermalExpansionCoefficient	NA	3.50E-05	1/K
thermal_expansion_TPTSPRIME	rock_thermalExpansionCoefficient	NA	3.50E-05	1/K
thermal_expansion_TRJN	rock_thermalExpansionCoefficient	NA	3.50E-05	1/K
thermal_expansion_TS	rock_thermalExpansionCoefficient	NA	3.50E-05	1/K
thermal_conductivity_x_QTA	thermalCond_effectiveConductivity	0	2.5	W/(m*K)
thermal_conductivity_y_QTA	thermalCond_effectiveConductivity	1	2.5	W/(m*K)
thermal_conductivity_z_QTA	thermalCond_effectiveConductivity	2	2.5	W/(m*K)
thermal_conductivity_x_QAS	thermalCond_effectiveConductivity	0	2.5	W/(m*K)
thermal_conductivity_y_QAS	thermalCond_effectiveConductivity	1	2.5	W/(m*K)
thermal_conductivity_z_QAS	thermalCond_effectiveConductivity	2	2.5	W/(m*K)
thermal_conductivity_x_TPTS	thermalCond_effectiveConductivity	0	3	W/(m*K)
thermal_conductivity_y_TPTS	thermalCond_effectiveConductivity	1	3	W/(m*K)
thermal_conductivity_z_TPTS	thermalCond_effectiveConductivity	2	3	W/(m*K)
thermal_conductivity_x_TPTSPRIME	thermalCond_effectiveConductivity	0	3	W/(m*K)
thermal_conductivity_y_TPTSPRIME	thermalCond_effectiveConductivity	1	3	W/(m*K)
thermal_conductivity_z_TPTSPRIME	thermalCond_effectiveConductivity	2	3	W/(m*K)
thermal_conductivity_x_TRJN	thermalCond_effectiveConductivity	0	3	W/(m*K)
thermal_conductivity_y_TRJN	thermalCond_effectiveConductivity	1	3	W/(m*K)
thermal_conductivity_z_TRJN	thermalCond_effectiveConductivity	2	3	W/(m*K)
thermal_conductivity_x_TS	thermalCond_effectiveConductivity	0	3	W/(m*K)
thermal_conductivity_y_TS	thermalCond_effectiveConductivity	1	3	W/(m*K)
thermal_conductivity_z_TS	thermalCond_effectiveConductivity	2	3	W/(m*K)

Table 2. Boundary conditions for H, T, and M.

# name	fieldName	component	setNames	scale	units	functionName
xconstraint	totalDisplacement	0	xneg;xpos;yneg;ypos	0	m	NA
yconstraint	totalDisplacement	1	xneg;xpos;yneg;ypos	0	m	NA
zconstraint	totalDisplacement	2	zneg	0	m	NA
edge_pressure	hydrostatic	.	yneg;ypos	.	.	edge_pressure
edgeTemperature	relative temperature	.	yneg;ypos	0	degC	NA
faultTemperature	relative temperature	.	fault_se_zneg	0	degC	NA
well_42_21_temperature	relative temperature	.	well_42_21	-94.3	degC	NA
well_43_21_temperature	relative temperature	.	well_43_21	-94.3	degC	NA
well_53_21_temperature	relative temperature	.	well_53_21	-94.3	degC	NA
well_25A_21	mass flux	.	well_25A_21	987	kg/s	well_25A_21
well_75B_16	mass flux	.	well_75B_16	926	kg/s	well_75B_16
well_76_16	mass flux	.	well_76_16	931	kg/s	well_76_16
well_42_21	mass flux	.	well_42_21	-987	kg/s	well_42_21
well_43_21	mass flux	.	well_43_21	-987	kg/s	well_43_21
well_53_21	mass flux	.	well_53_21	-987	kg/s	well_53_21
well_61_21	mass flux	.	well_61_21	923	kg/s	well_61_21

FIGURES

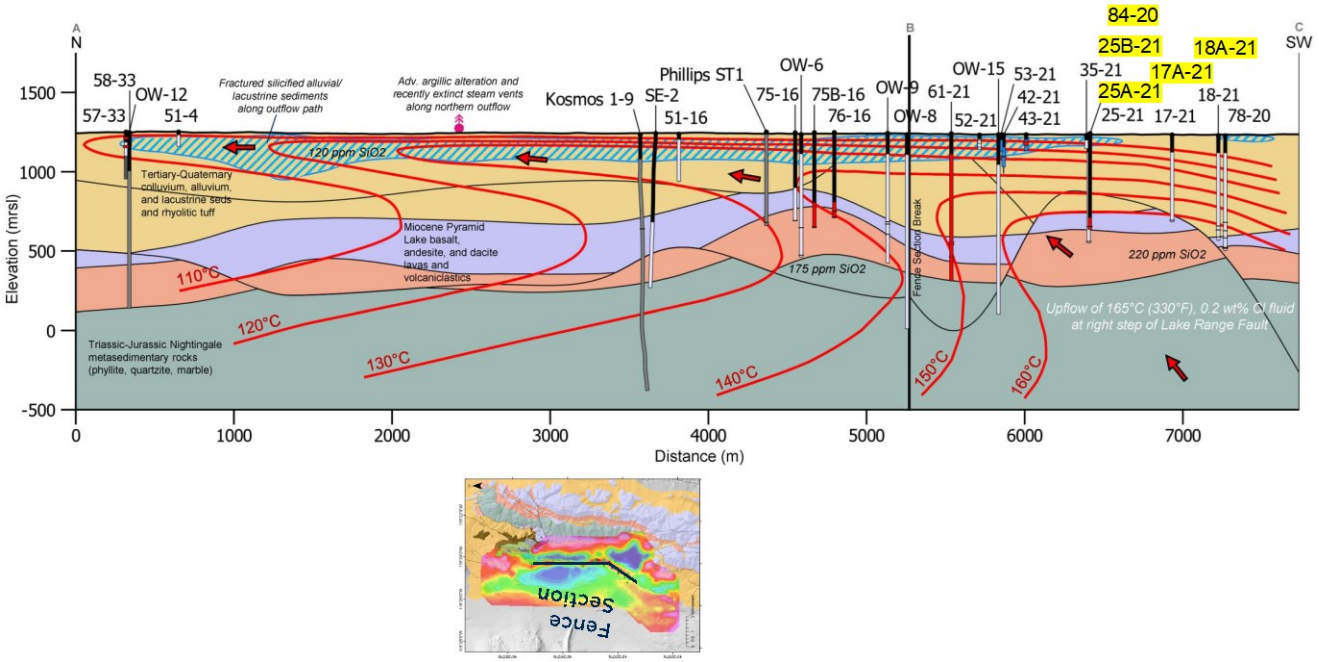

Figure 1: Vertical cross section of conceptual model of WHOLESCALE study area at San Emidio, showing geologic units (color), wells (vertical line segments, black where cased, white where open, red where tapping feed zone), and contours of "native state" temperature (red curves) (Folsom et al., 2020). The cross section follows the two black line segments shown in map view (lower panel) with a bend at point B. Names of wells are indicated (highlighted in yellow if drilled since 2020).

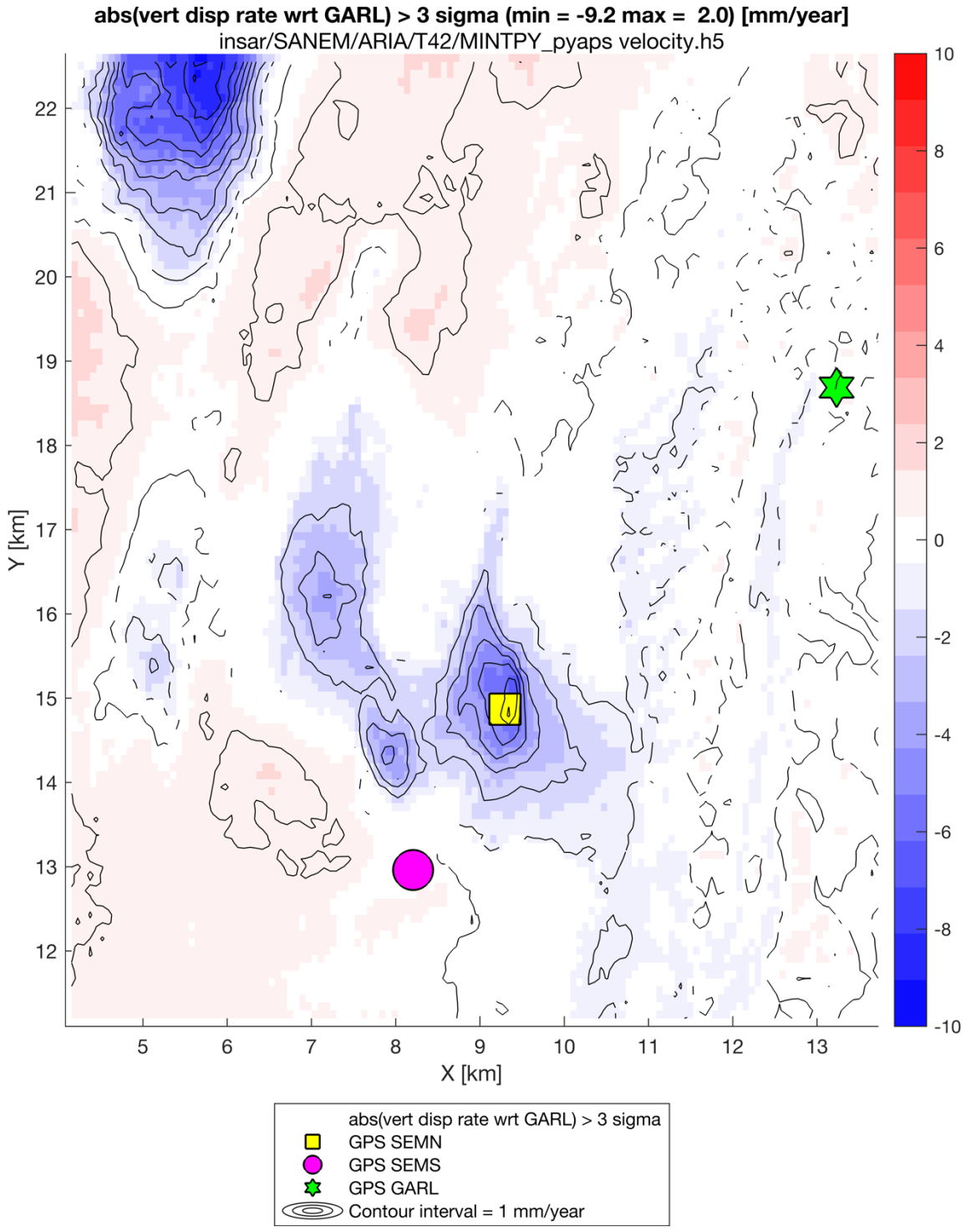

Figure 2. Map of the rate of vertical displacement estimated from InSAR data acquired between 2016 and 2022 by the Sentinel-1 satellite mission in Track 42. The rate of vertical displacement has been estimated using MintPy, neglecting atmospheric effects. The rates mapped in colors are referred to the median of the values for pixels located near GPS station GARL. Upward motion (relative uplift) appears as reddish colors, downward motion (relative subsidence) appears as blueish colors. Note the different color scales in each panel. Colors show only rates with an absolute value greater than 3 times their formal standard deviation. Symbols show GPS stations SEMS (yellow square), SEMN (magenta circle), and GARL (green star). Contour interval is 1 mm/year. Coordinates are in km with respect to an origin at UTM (Easting, Northing) = (286.924, 4457.967) [km].

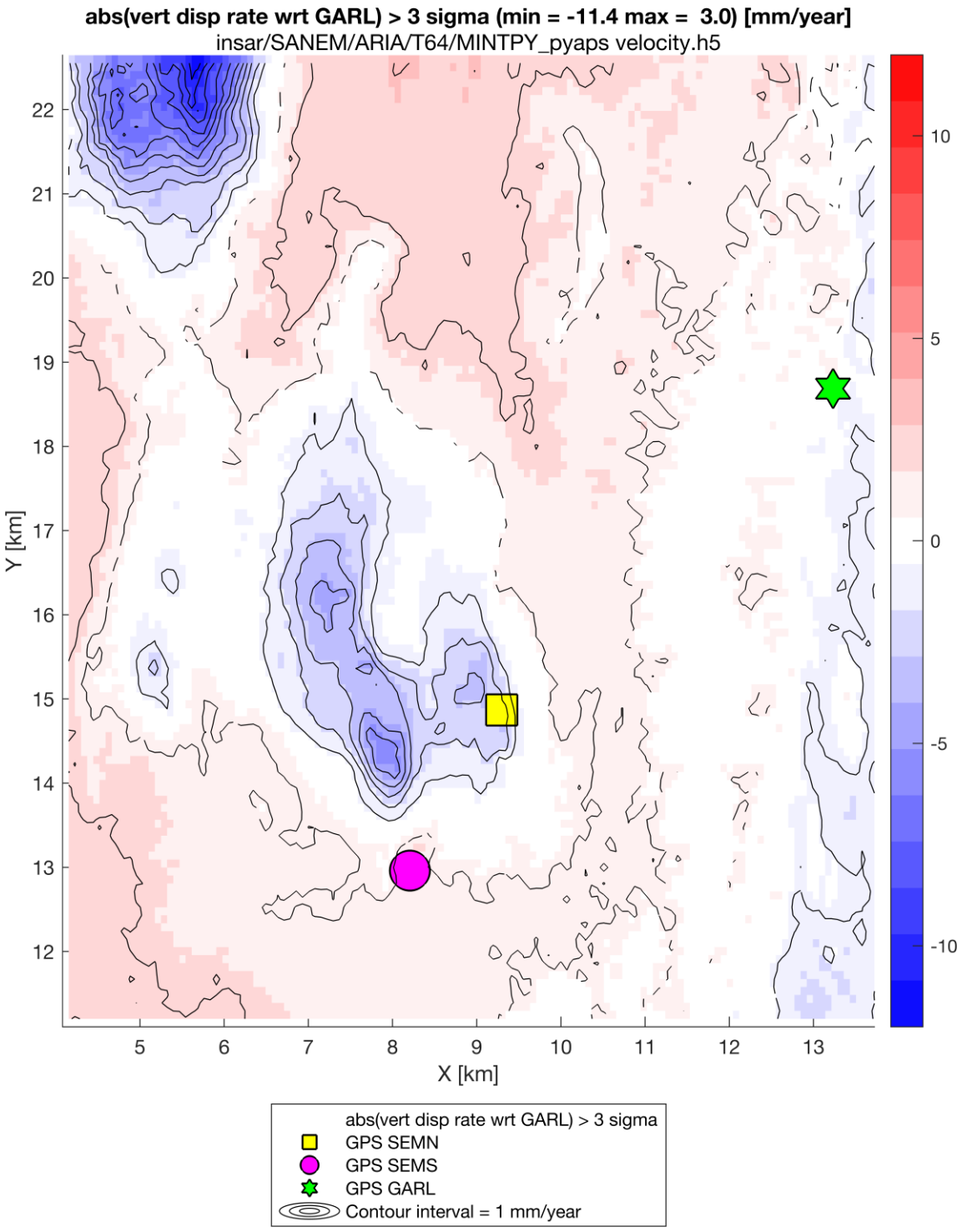

Figure 3. Map of the rate of vertical displacement estimated from InSAR data acquired between 2016 and 2022 by the Sentinel-1 satellite mission in Track 64. Plotting conventions as in previous figure.

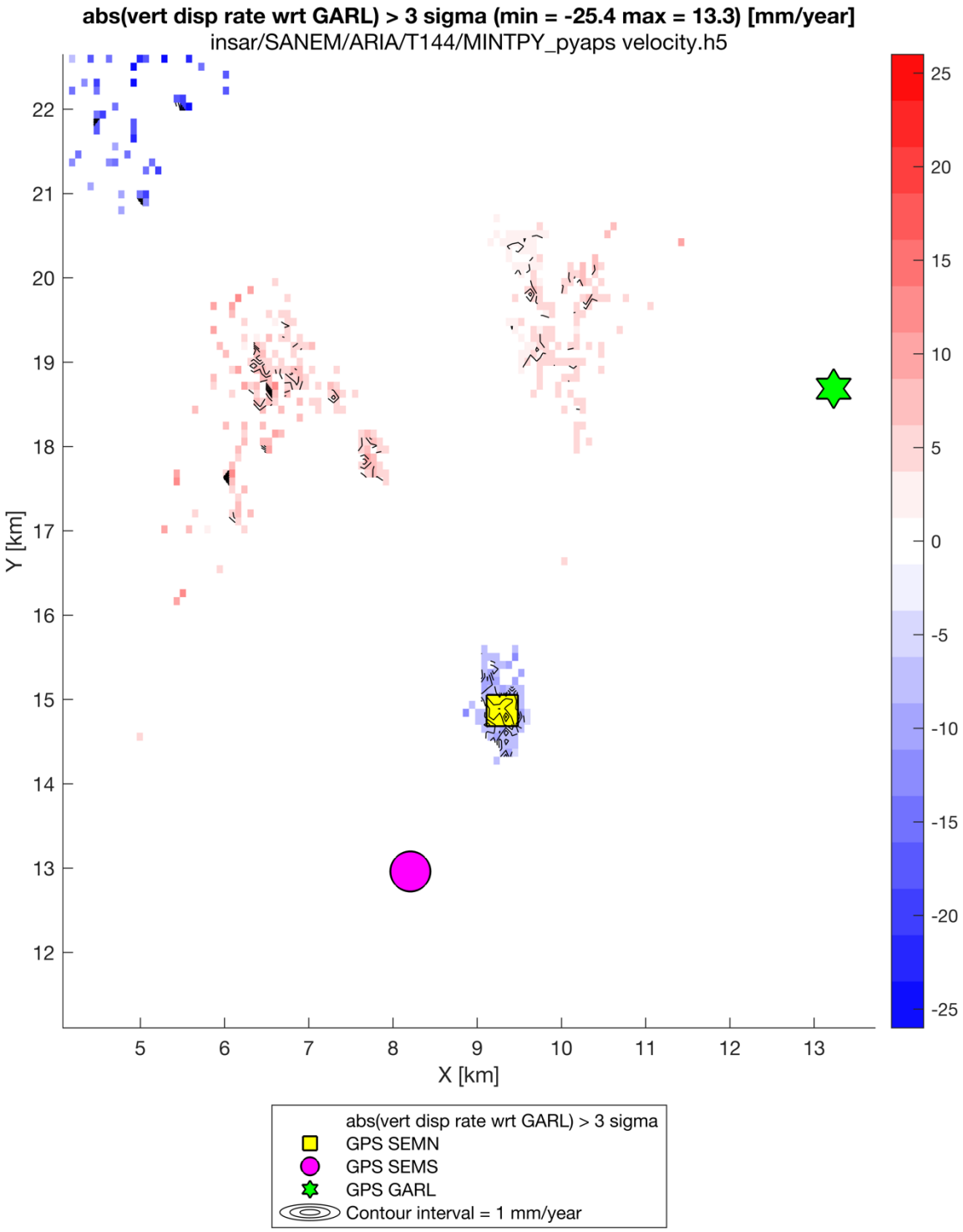

Figure 4. Map of the rate of vertical displacement estimated from InSAR data acquired between 2016 and 2022 by the Sentinel-1 satellite mission in Track 144. Plotting conventions as in previous figures.

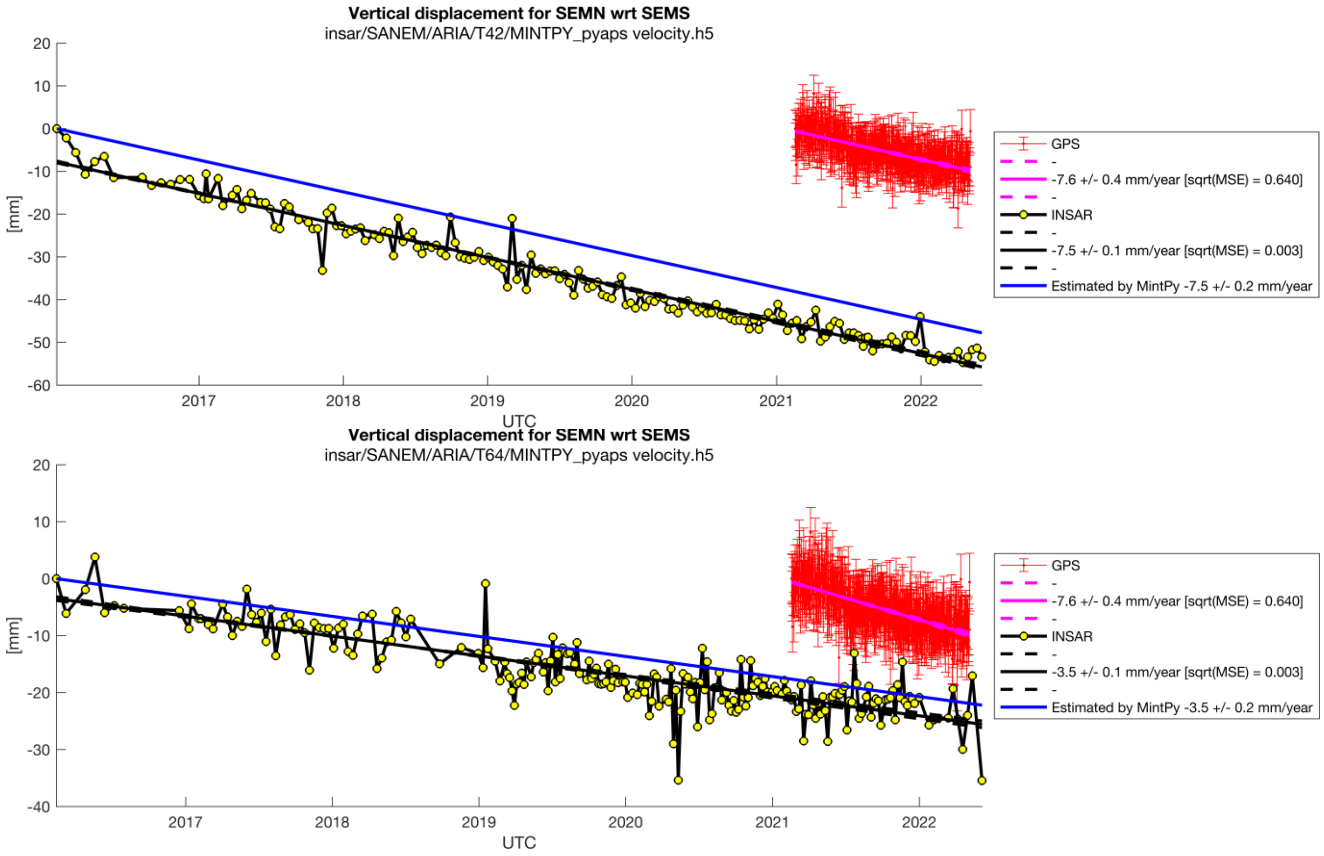

Figure 5. Time series of relative vertical displacement estimated from InSAR and GPS data for a point located near GPS station SEMN with respect to a point located near GPS station SEMS. The InSAR data were acquired by the Sentinel-1 satellite mission in Track 42 (upper panel) and Track 64 (lower panel). In each panel, the yellow circles connected by black line segments represented the displacement at the date of each InSAR acquisition. In each panel, the blue line best fit to the InSAR data estimated using unweighted least squares. The black line shows the rate of vertical displacement estimated from the InSAR data by MintPy, neglecting atmospheric effects. The red points with 1-σ error bars show the vertical component of displacement measured from GPS data analyzed by the Nevada Geodetic Laboratory at the University of Nevada-Reno (Blewitt et al., 2018; Kreemer et al., 2020). The magenta line shows the best fit to the GPS data estimated using weighted least squares. The GPS data and estimates are identical in both panels. The Y-intercepts of the GPS and InSAR data sets are arbitrary.

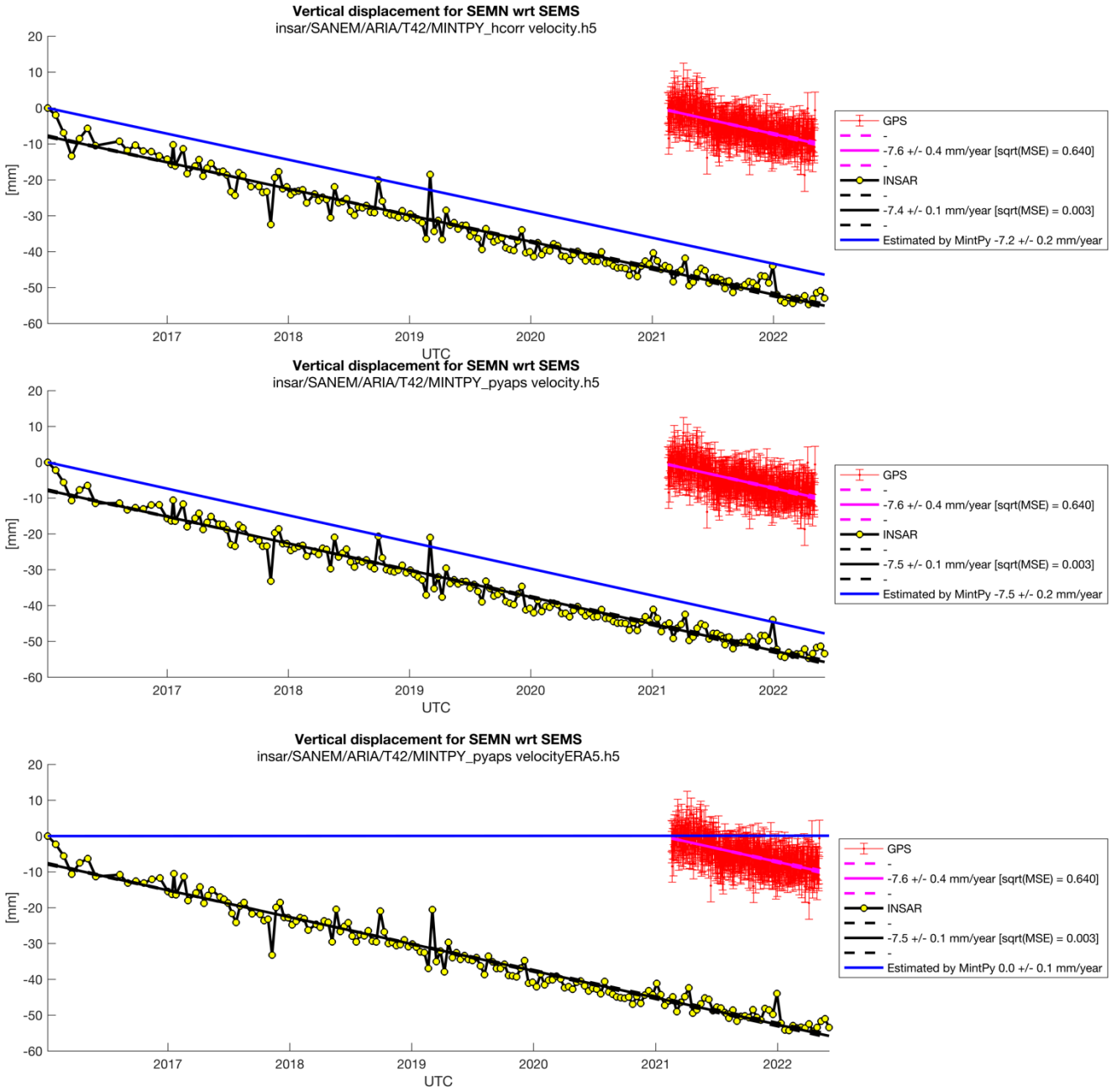

Figure 6. Time series of relative vertical displacement estimated from InSAR data acquired by the Sentinel-1 satellite mission in track 64 (yellow circles connected by black line segments). The three panels show results estimated using three different approaches for mitigating atmospheric effects: (upper panel) height-correlation; (middle panel) neglecting atmospheric effects, and (lower panel) PyAPS with meteorologic data. In each panel, the blue line best fit to the InSAR data estimated using unweighted least squares. The black line shows the rate of vertical displacement estimated from the InSAR data by MintPy. The red points with 1-σ error bars show the vertical component of displacement measured from GPS data analyzed by the Nevada Geodetic Laboratory at the University of Nevada-Reno (Blewitt et al., 2018; Kreemer et al., 2020). The magenta line shows the best fit to the GPS data estimated using weighted least squares. The GPS data and estimates are identical in both panels. The Y-intercepts of the GPS and InSAR data sets are arbitrary.

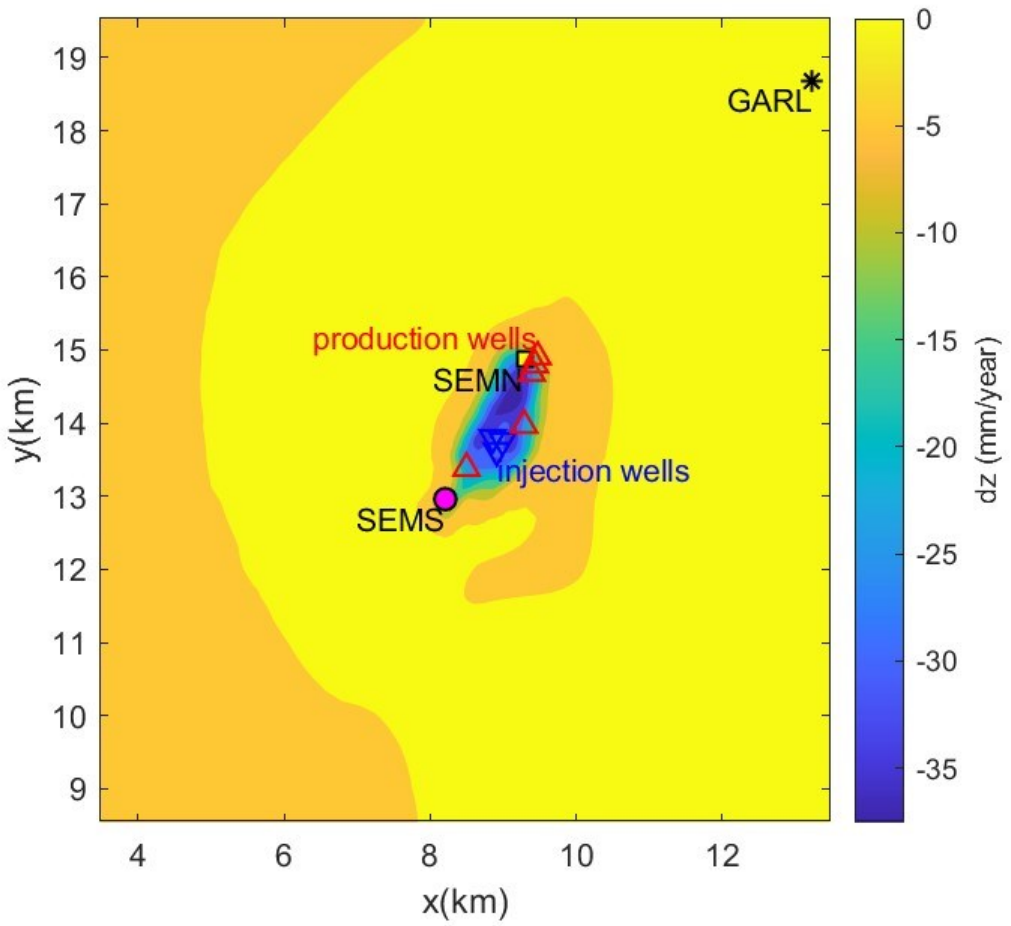

Figure 7. Map view of rate of vertical displacement as calculated by a GEOS simulation of a T-H-M model starting in 2010. Red and blue triangles indicate production and injection wells. Other symbols show GPS stations SEMS (yellow square), SEMN (magenta circle), and GARL (gray asterisk).

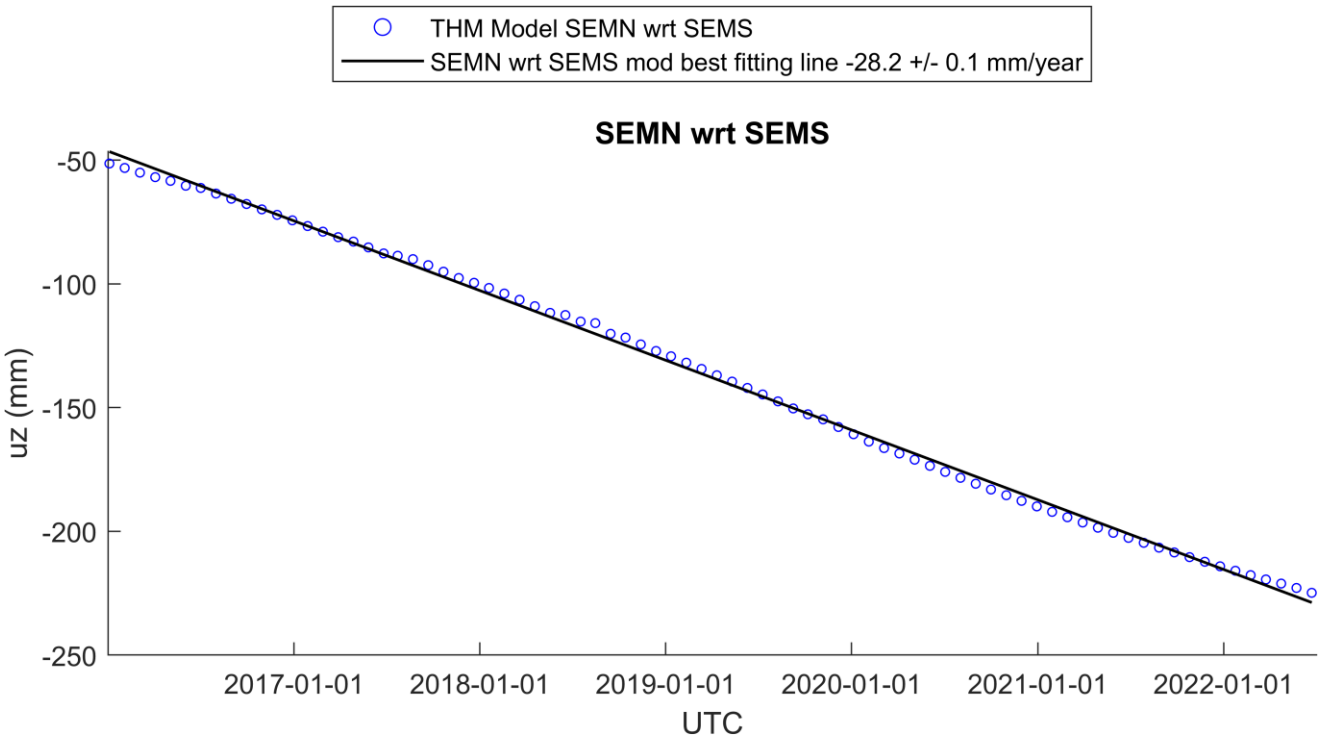

Figure 8. Time series of vertical displacement in millimeters of a point located near GPS station SEMN with respect to a point located near GPS station SEMS as calculated by a GEOS simulation of a T-H-M model.